Temperature-dependence of hypersound dynamics in $SrRuO_3/SrTiO_3$ heterostructures

Chi-Yuan Yang (楊濟源)[1,2,3] and Kung-Hsuan Lin (林宮玄)[3,*]
[1]*Department of Physics, National Taiwan University, Taipei 10617, Taiwan*
[2]*Nano-Science and Technology Program, Taiwan International Graduate Program, Academia Sinica, Taipei 11529, Taiwan*
[3]*Institute of Physics, Academia Sinica, Taipei 11529, Taiwan*

(Received 2 November 2017; revised manuscript received 15 August 2018; published 29 August 2018)

We studied GHz hypersound in heterostructures of $SrRuO_3$ (SRO) and $SrTiO_3$ (STO) by using femtosecond pulses with fluence as low as several tens of $\mu J/cm^2$. We found that the efficiency of generating hypersound in SRO, through thermal expansion, is linear up to optical fluence of a few mJ/cm^2. We further investigated the propagation of acoustic pulses in the STO substrate. The acoustic properties of STO dramatically changed around the temperature of structural transition (105 K) because the generated hypersound was coupled to the softening mode. Nevertheless, our experimental results revealed that the quadratic frequency dependence of acoustic attenuation in STO, predicted by the mode-coupling theory, breaks down at tens of GHz. Finally, the refractive index of STO was experimentally obtained between 365 and 400 nm, for which there was disagreement in previous results.

DOI: 10.1103/PhysRevB.98.064308

I. INTRODUCTION

Strontium ruthenate ($SrRuO_3$, SRO) and strontium titanate ($SrTiO_3$, STO) are both complex oxides with perovskite structures and have been widely studied for their exotic properties, including superconductivity, thermoelectricity, and interfacial anomalies [1,2]. STO undergoes a structural phase transitions around 105 K and exhibits interesting behaviors related to dielectric permittivity and ferroelectricity at even lower temperatures [3,4]. The structural evolution of STO around structural phase transition has been studied with ultrasonic spectroscopy at MHz frequencies [5–7]. Recently, complex-oxide heterostructures, with high quality, have been successfully grown on the STO substrates by pulsed laser deposition (PLD). SRO thin film has received significant amount of attention because of its high absorption in visible range and metallic properties [8]. For example, SRO thin film could serve as an acoustic transducer to generate acoustic pulses with bandwidth up to 100 GHz [9–16] for hypersonic spectroscopy.

Metal thin films were first utilized as acoustic transducers to photoexcite hypersound [17,18]. By shining femtosecond optical pulses, longitudinal acoustic pulses can be launched in metals via thermal expansion. This technique is called picosecond ultrasonics [19,20] and have been widely applied to acoustic studies of materials on the order of 100 GHz. Semiconductor heterostructures were later demonstrated to achieve acoustic frequencies up to THz regime [21–28] because the acoustic generation is primarily through the processes such as piezoelectric effects [21–26] and deformation potential couplings [27,28], which are faster than thermal expansion. The acoustic waveform and frequency response can also be engineered by the design of heterostructures [29]. However, there are limited materials, which can be grown on the semiconductor heterostructures (such as material systems based on GaN or GaAs) for acoustic studies. In contrast, more materials can be studied by coating metal thin films as the acoustic transducers, although the bandwidth is relatively low. Thanks to the success of PLD for epitaxial growth of complex oxide films, SRO-based heterostructures are emerging transducers to generate hypersound. They open possibilities to investigate acoustic properties of a variety of perovskite materials by taking the advantages of heterostructures such as waveform engineering.

Acoustic pulses with strain 10^{-3} to 10^{-2} were generated in SRO by using optical pulses with fluences on the order of $10\,mJ/cm^2$ [9–14], and such large strain was close to the regime of nonlinear acoustics [13]. Recently, photoinduced strain of SRO was observed up to and saturated at 10^{-2} under excitation of continuous-waves with low instantaneous optical density compared with femtosecond pulses [30]. Because the optical intensity of the continuous-waves is much lower than that of the femtosecond pulses, it is intriguing if acoustic pulses with large strain could be generated in SRO by weak pulses such as a few tens of $\mu J/cm^2$? Is the generation efficiency of acoustic pulses already saturated under excitation of strong pulses on the order of a few mJ/cm^2 in the literature [9–14]? In this work, we have utilized weak femtosecond pulses to generate hypersound in SRO/STO heterostructures for the first time. We found that the efficiency of generating hypersound in SRO, through thermal expansion, is linear up to optical fluence of a few mJ/cm^2. We have also studied the temperature dependence of coherent phonon dynamics in STO. The quadratic frequency dependence of acoustic attenuation in STO, predicted by the mode-coupling theory [31], breaks down at tens of GHz. Finally, we have experimentally obtained the refractive index of STO substrate between 365 and 400 nm, for which there was disagreement in previous results [32,33].

*linkh@sinica.edu.tw

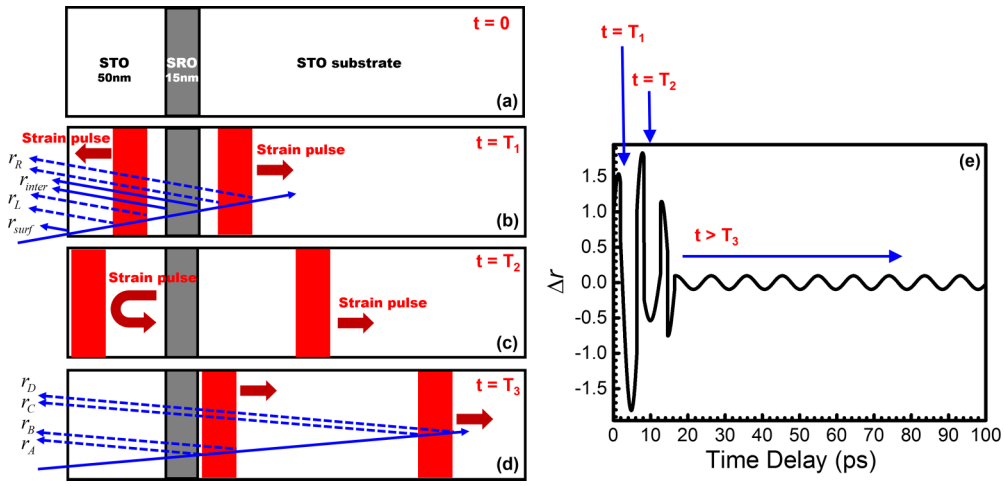

FIG. 1. Schematics of (a) the sample structure, (b) both acoustic pulses just being launched from SRO, (c) the left-propagating acoustic pulse being reflected from the surface, and (d) the acoustic pulses both propagating in the STO substrate. (e) Calculated optical reflection changes due to the propagation of acoustic pulses. The oscillation becomes single sinusoidal function after $T_3 = 18$ ps.

II. EXPERIMENTAL METHODS AND PRINCIPLES

Optical pulses, from a Ti:sapphire oscillator (Tsunami HP, Newport Inc.), were used for pump-probe measurements. The duration and repetition rate of the optical pulses were around 150 fs and 80 MHz. Two types of experimental setup were used for investigation. For the first one, the frequency-doubled optical pulses (by using a BBO crystal) were split into pump and probe pulses. Degenerate pump-probe measurements were conducted for pump/probe wavelengths between 365 and 400 nm at room temperature by tuning the central wavelength of the Ti:sapphire oscillator from 730 to 800 nm. Temperature-dependent measurements were further conducted at 400 nm. The sample was placed in a cryostat, and the pressure of the chamber was kept at 10^{-6} torr. After the sample was cooled down to 77 K, the measurements were conducted from 77 to 300 K. The pump fluences were kept the same for all temperatures. For the second type of experimental setup, non-degenerate geometry with pump (400 nm) and probe (800 nm) were utilized. Temperature-dependent measurements were conducted in a similar method. For all the measurements, the reflection changes of the probe pulses were recorded as a function of time delay between the pump and probe. The optical pump fluence was $\sim$60 μJ/cm^2 and the diameter of the optical spot was $\sim$25 μm on the sample.

The schematic of Fig. 1(a) shows the sample structure. The SRO film (15 nm) is sandwiched by the top STO film (50 nm) and the STO substrate. All of the crystal orientations are along (001). After the optical pulses excite carriers in the SRO film, two initiated strain-pulses propagate in counter directions as shown in Fig. 1(b). After the strain pulse, toward the surface, is bounced back, it propagates toward the STO substrate as shown in Fig. 1(c). The strain pulses will eventually both propagate in the STO substrate as shown in Fig. 1(d). Since the longitudinal sound velocities of SRO and STO along (001) direction are 6.31 nm/ps [14,34] and 7.9 nm/ps [35,36], the strain pulses both propagate in the STO substrate after $\sim$18 ps.

The optical reflection changed by propagation of strain pulses can be calculated with a simplified model [37,38] as follows. The strain pulses are assumed as square pulses which induce homogeneous changes of optical constant $\delta\tilde{n}_k$, where the subscript k denotes STO or SRO. The summation of reflection amplitudes in Fig. 1(b) can be represented as

$$r = r_R + r_{\text{inter}} + r_L + r_{\text{surf}} + O(\delta\tilde{n}^2), \tag{1}$$

where r_{inter} and r_{surf} are the background reflections from the interfaces of SRO/STO and the surface, respectively. r_R and r_L are the reflections from the moving interfaces due to the strain pulses toward right and left directions, respectively. Here, the Fabry-Perot series of multiple reflections are neglected as indicated by $O(\delta\tilde{n}^2)$ in Eq. (1). Because only r_R and r_L varies as a function of time, the total reflection changes can be simplified as

$$\Delta r \propto r_L + r_R = (r_A + r_B) + (r_C + r_D), \tag{2}$$

where $r_L = r_A + r_B$ and $r_R = r_C + r_D$ as shown in Fig. 1(d). With consideration of each light path,

$$r_j \propto e^{2ik_k z_j}\delta\tilde{n}_k, \tag{3}$$

where the subscript j represents the interfaces A, B, C, or D. k_k is the wavenumber of the light in the media denoted by the subscript k, which can be STO, SRO, or air. z_j is the distance between the interface j and the surface.

Figure 1(e) shows the calculated results following Eqs. (2) and (3). The oscillations before T_3 are complicated due to several factors. First, the sign of the strain pulse will be reversed upon reflection at the surface. While the strain pulse, heading to left direction, encounters the surface, the $\delta\tilde{n}_{\text{STO}}$ reverses the sign leading to sign changes of r_A and r_B as shown in Fig. 1(c). Second, the optical intensity decreases after the light travels through the absorbing SRO film [39]. The amplitudes of r_L and r_R thus greatly differ with each other when the strain pulses are on different sides of the SRO film as shown in Figs. 1(b) and 1(c). When the strain pulse passes through the SRO thin film, it induces dramatic changes of r_L (or $r_A + r_B$). Third, the phase of $\delta\tilde{n}_k$ is different between the metallic SRO and transparent STO [37,40]. r_A and r_B significantly varies while the strain pulse is crossing the SRO thin film. In contrast to the aforementioned conditions, the oscillation after T_3 (18 ps

for our sample) in Fig. 1(e) is simply sinusoidal. When the strain pulses both propagate in the STO substrate as shown in Fig. 1(d), z_j in Eq. (3) becomes the only variable as a function of time if we neglect the attenuation of strain pulse in the STO substrate. It results in oscillations with single frequency f, which is Brillouin frequency. The frequency f can be represented as

$$f = \frac{2nV\sin\theta}{\lambda}, \tag{4}$$

where n and V are the refractive index and sound velocity of the STO substrate. λ is the wavelength of the probe beam, and θ is the incidence angle of light inside the sample.

Because the attenuation of acoustic pulses and the optical absorption in STO are not considered, the amplitude of oscillations in Fig. 1(e) keeps the same after T_3. Since the absorption coefficient of bulk STO is $4\,\mathrm{cm}^{-1}$ [41] at 3.1 eV (400 nm), corresponding to penetration depth of 2.5 mm, it is reasonable to ignore the light absorption of STO for probe wavelength 400 and 800 nm in our experimental conditions. Therefore, we can simply analyze the relaxation of Brillouin oscillations to characterize the attenuation of the acoustic pulses [20,42]. Note that the Brillouin oscillations only reflect the properties of the acoustic frequency f in Eq. (4) although the generated strain pulses are composed of a band of frequency. In this work, we analyze the Brillouin oscillations after 18 ps to investigate phonon generation in SRO and acoustic properties of STO at the Brillouin frequency. By using different probe wavelengths such as 400 and 800 nm, acoustic properties at frequencies such as ~105 and ~45 GHz can be investigated.

III. RESULTS AND DISCUSSIONS

Figure 2 shows the result of transient reflection with pump/probe wavelengths of 400/400 nm at room temperature. After zero time delay, oscillations with frequency around 100 GHz are carried on the exponential-decay-like relaxation curve. The "background" curve is dominated by the carrier dynamics in the metallic SRO because the pump pulses, with photon energy 3.1 eV (corresponding to 400 nm), can only excite few carriers in STO (with bandgap of ~3.2 eV) through

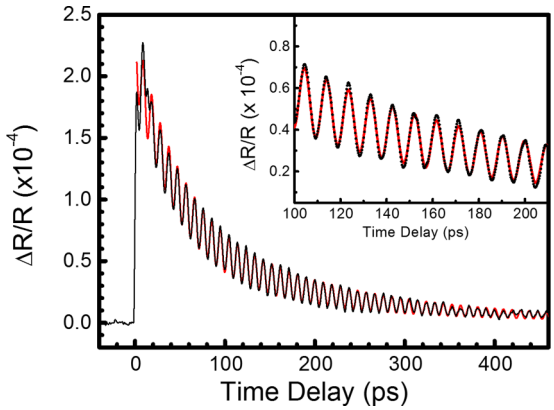

FIG. 2. The solid dots depict the measured reflection changes of the probe pules as a function of pump-probe (400–400 nm) time delay at room temperature. The fitting curves are represented by red lines. The inset zooms in the curves to reveal the good quality of fitting.

two-photon absorption. This decay curve reflects the duration that the excited carriers relax to the Fermi surface of SRO. The Brillouin oscillations on the "background signal" were extracted by fitting the trace in Fig. 2 as follows:

$$\frac{\Delta R}{R}(t) = \sum A_i \exp(-t/\tau_i) + A_P \times \exp(-t/\tau_P)\sin(2\pi f t - \phi), \tag{5}$$

where the second term on the right-hand side represents the Brillouin oscillations. A_P and τ_P specify the amplitude and decay time of the Brillouin oscillation signals. $\sin(2\pi f t - \phi)$ is the oscillation term with a phase delay ϕ. Overall, the red curve in Fig. 2 fits well with the experimental data after 20 ps. As discussed in Sec. II, the optical reflection changes can be adequately fitted with the damped sinusoidal function when the strain pulses both propagate in the STO substrate after T_3 (18 ps for our sample) in Figs. 1(d) and 1(e). The zoom-in, in the inset of Fig. 2, further reveals the good quality of fitting. The results of fitting in Fig. 2 indicate that $f = 105$ GHz and $\tau_P = 207$ps, representing that the phonon lifetime of the STO substrate is 207 ps at 105 GHz.

The obtained $A_P = 1.7 \times 10^{-5}$ in Eq. (5) represents the modulation depth of the optical interference. In such a small perturbation regime, the modulation depth can be treated linear to the changes of the refractive index, that is, $\Delta n \sim 1.7 \times 10^{-5}$. Based on the estimation from the photoelastic effects in STO [43], the strain of the hypersound is on the order of 10^{-5} at acoustic frequency $f = 105$ GHz. In contrast to the transient strain in the literature [9–13], which is around 10^{-3}–10^{-2} under excitation with pulse fluence of $10\,\mathrm{mJ/cm^2}$, both the optical fluence and the generated strain under our experimental conditions are two order of magnitude low. Therefore, our results reveal that the phonon generation in SRO should be linear with pulse fluence up to a few $\mathrm{mJ/cm^2}$. After the electrons are excited in SRO, electron-electron scatterings are followed by the electron-phonon scatterings. The nonequilibrium phonons result in thermal expansion and initiate strain pulses propagating in counter direction as shown in Fig. 1(b). This mechanism of generating strain pulses in SRO is similar to that in metal.

We kept the same experimental conditions of Fig. 2 and conducted temperature-dependent experiments to study the generation efficiency of strain pulses in SRO. Similar to Fig. 2, we used Eq. (5) to fit the traces at different temperatures. Figure 3(a) shows the temperature dependence of the extracted A_P described in Eq. (5), which is proportional to the amplitude of the hypersound strain around 100 GHz. The amplitudes of strain amplitude below 100 K are roughly a half of those above 200 K. We have confirmed that the reduction of strain below 100 K is not caused by the temperature dependence of optical absorption. The absorption rate of SRO is associated with the term $\sum A_i \exp(-t/\tau_i)$ in Eq. (5), which describes the carrier dynamics in SRO. Under the same excitation fluence, Fig. 3(b) shows the temperature dependence of $\sum A_i$, which reflects the trend of absorption rate. It reveals the absorption rate of SRO is relatively high below 100 K. According to Figs. 3(a) and 3(b), the generated strain amplitudes from SRO at 100 K are weaker than those above 200 K even though SRO has relatively high absorption at 100 K. It should be noted that SRO exhibits

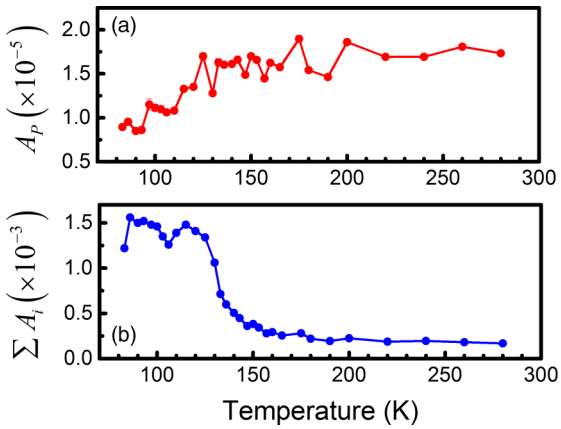

FIG. 3. The temperature dependence of (a)A_P and (b)$\sum A_i$. A_P is proportional to the hypersound strain at 105 GHz generated in the SRO. The summation of A_i is associated with the carrier density excited in the SRO. Detailed description of the parameters A_P and A_i in Eq. (5) can be found in the main text. Note that most error bars, from the standard deviation errors of fitting, are short and embedded in the solid dots.

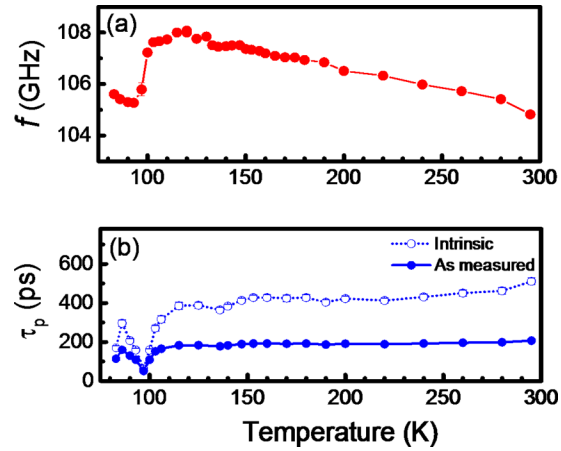

FIG. 4. The temperature dependence of (a) Brillouin oscillation frequency and (b) phonon lifetime obtained by fitting the experimental data of pump-probe (400–400 nm) measurements. The solid dots represent the as measured phonon lifetimes. The open circles represent the intrinsic phonon lifetimes. Note that most error bars, from the standard deviation errors of fitting, are short and embedded in the solid dots and open circles.

paramagnetic phase at room temperature but ferromagnetic phase below the Curie temperature ~150 K [9]. When SRO is in ferromagnetic phase such as below 100 K, the magnetostrictive effects induce transient compression stress upon photoexcitation of femtosecond pulses, and compensate the out-of-plane transient thermal expansion [9]. The generation efficiency of the strain pulses in SRO is thus reduced below 150 K because of the additional magnetostrictive effects below the Curie temperature of SRO.

It is intriguing that photoinduced static-strain in SRO can be as large as 10^{-2} under photoexcitation of continuous waves [30]. Such a huge strain should be generated by strong femtosecond pulses with optical intensity several orders higher than that of continuous waves. But our experimental results rule out the possibility that the optical fluence of a few mJ/cm^2 saturates the efficiency of phonon generation. We therefore conclude that the large strain induced by the continuous waves is caused by another mechanism with slow response in addition to the thermal expansion and magnetostriction with responses within 1 ps. The deformation should result from consistent interaction between the excited electrons and lattices under excitation of continuous waves, leading to accumulated static-strain reaching to 10^{-2}. In our work, the "background" curve in Fig. 2 indicates that the photoexcited electrons relax into ground states within a few hundred picoseconds. The interaction in such a short duration could not initiate strong strain. Our experimental results reveal that it should take interaction duration, much longer than tens of picoseconds, to induce the strain up to and saturate at 10^{-2}. The precise response time requires novel design of experiments, which is out of the scope of this work.

Figure 4(a) shows the temperature dependence of the extracted f in Eq. (5), which reveals the structural properties of the STO substrate. When the temperature decreases from 295 to 105 K, the frequency monotonically increases 3% from 105 to 108 GHz. The variations of Brillouin frequency f could result from several parameters such as the probe wavelength (λ), incident angle of light (θ), refractive index (n), and sound velocity (V) in Eq. (4). Because the experimental geometry for different temperatures (T) is the same, the wavelength and incident angle of light can be first ruled out. Regarding the refractive index, we assume that dn/dT is -10^{-4} K^{-1} [44] from 295 to 105 K. Due to dn/dT, the Brillouin frequency could vary 0.7% within this temperature range. But it cannot completely account for the 3% variations of Brillouin frequency in Fig. 4(a). After calibration of the effects from refractive index, the longitudinal sound velocity of STO should increase 2.3% from room temperature to 105 K. The sound velocity $V = \sqrt{C_{33}/\rho}$, where C_{33} and ρ are stiffness and mass density, respectively. The temperature-dependent variation of ρ can be ignored because the thermal expansion coefficient of STO, which is associated with volume and mass density, is $\sim 2 \times 10^{-5}$ K^{-1} [3]. Therefore, the variation of sound velocity is primarily caused by the temperature dependence of C_{33}. Since $C_{33} \propto V^2$, the stiffness of STO along (001) direction increases ~4.6% from room temperature to 105 K.

Figure 4(a) also reveals an abrupt frequency change around 100 K, which is close to the temperature of structural transition from cubic to tetragonal structure. The Brillouin frequency is ~108 GHz at 110 K for cubic structure but decreases to ~105 GHz at 90 K for tetragonal structure. The Brillouin frequency drops abruptly 2–3% within this small temperature range. The solid dots in Fig. 4(b) represent the extracted τ_P, which indicates the phonon lifetime (or acoustic attenuation) at the Brillouin frequency. The temperature dependence of τ_P also exhibits dramatic change around the structural transition temperature. These features of abrupt changes in stiffness and acoustic attenuation are similar to those observed by ultrasonic measurements with frequency on the order of 100 MHz [5–7]. Note that STO actually undergoes second-order phase transition rather than first-order with a discontinuous change at transition. During the structural transition of STO, oxygen octahedrons rotate about the crystal axis, leading to

diminishing bonding forces and crystal softening [45]. Investigations of STO with neutron scattering [46] reveal that the frequency of the phonon Γ_{25} mode at the R point continuously decreases from 700 GHz at 150 K down to below the limit of instrument 250 GHz at the transition temperature ∼105 K. While the temperature further goes down to 90 K, the frequency of Γ_{25} mode becomes measurable above the instrument limit, and slowly increases with decreasing temperature from 90 K. Coupling between this Γ_{25} soft mode and the ultrasound [31] accounts for the experimental results in MHz regime [5–7]. This can also qualitatively explain the drop of ∼100 GHz phonon lifetime around the transition temperature ∼105 K in Fig. 4(b). When the temperature is cooled down to 105 K, the frequency of the phonon Γ_{25} mode at the R point continuously softens and reaches zero frequency. If the frequency of Γ_{25} phonon mode is close to the frequency of GHz hypersound we observe, coupling between both modes is dramatically enhanced. The hypersound, at resonance with the frequency of Γ_{25} mode, thus damps quickly through mode coupling, and exhibits high attenuation and low phonon lifetime around the structural transition temperature of STO.

The mode-coupling theory [31] also predicts that $\tau_P^{-1} \propto f^2$ at the same temperature. To further evaluate the validity of quadratic dependence of frequency in GHz regime, we additionally conducted transient reflection measurements with pump/probe wavelengths of 400/800 nm. According to Eq. (4), the Brillouin frequency is 46–47 GHz when the probe wavelength is 800 nm. We conducted two sets of temperature-dependent measurements. The temperature of the first set is close to the structural transition temperature 105 K. The second set of measurements was conducted between 150 and 295 K. Similarly, we fitted the curves with Eq. (5) to obtain the parameters such as f and τ_P. The solid dots in Figs. 5(a) and 5(c) represent the extracted f and τ_P between 90 and 110 K. The solid dots in Figs. 5(b) and 5(d) represent the extracted f and τ_p above 150 K, respectively. The overall trends of temperature dependence in Fig. 5 for ∼46 GHz are

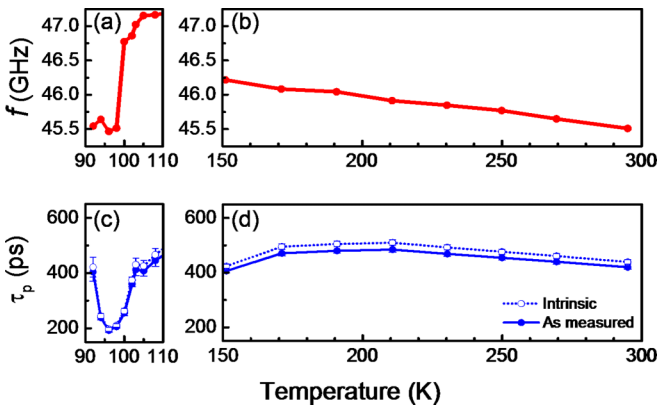

FIG. 5. The solid dots depict the (a, b) Brillouin oscillation frequency and (c, d) phonon lifetime obtained by fitting the experimental data of pump-probe (400–800 nm) measurements. The open circles in (c, d) represent the intrinsic phonon lifetimes. Most error bars, from the standard deviation errors of fitting, are short and embedded in the solid dots and open circles. Note that (a, c) and (b, d) were obtained from different sets of temperature-dependent measurements.

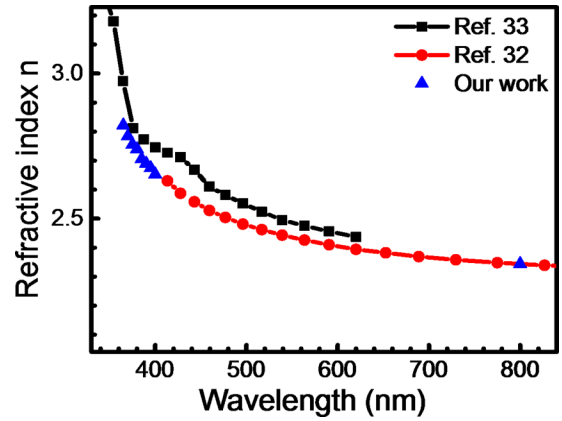

FIG. 6. The refractive index of STO experimentally obtained from Refs. [32], [33], and our work at room temperature.

qualitatively the same with those at ∼100 GHz in Fig. 4. The phonon lifetime of ∼46 GHz also dramatically drops around the transition temperature due to the aforementioned coupling with phonon Γ_{25} mode at the R point. However, the as measured phonon lifetimes of Figs. 4(b) and 5(d) are ∼200 ps (for 105 GHz) and ∼400 ps (for 46 GHz), respectively. They do not follow the quadratic dependence of frequency $\tau_P^{-1} \propto f^2$ as predicted by the mode-coupling theory.

The as measured τ_p in Figs. 4(b) and 5(d) should not reflect the intrinsic phonon lifetime if defect scatterings are significant. We further consider the effects of defect scatterings to recover the intrinsic phonon lifetimes. The as measured τ_P should follow the Matthiessen's rule:

$$\frac{1}{\tau_p} = \frac{1}{\tau_{\text{in}}} + \frac{1}{\tau_{\text{ex}}}, \tag{6}$$

where τ_{in} and τ_{ex} are the intrinsic and extrinsic lifetimes. Here, we assume that τ_{ex} is dominated by the defect scatterings especially point defects such as oxygen vacancies. A recent investigation reports that the phonon lifetime of high purity STO (99.99%) is 480 ps at ∼100 GHz [20], which should be close to the intrinsic lifetime. According to Eq. (6), we assume that τ_{in} is 480 ps for 105 GHz at 295 K and obtain τ_{ex}. Because τ_{ex} should be independent to the temperature, the intrinsic phonon lifetimes as a function of temperature can thus be recovered as represented by open circles in Fig. 4(b).

The intrinsic lifetimes in Figs. 5(c) and 5(d) can further be recovered based on the assumption that the scattering rate of Rayleigh-like defects $\tau_{\text{ex}}^{-1} \propto f^4$. The open circles in Figs. 5(c) and 5(d) represents the recovered intrinsic lifetimes. There are no significant differences between the intrinsic lifetimes and the as measured lifetimes because τ_{ex} is on the time scales of a few nanoseconds and $\tau_{\text{in}}^{-1} \simeq \tau_p^{-1}$ if $\tau_{\text{ex}}^{-1} \gg \tau_p^{-1}$ in Eq. (6). As shown in Figs. 4(b) and 5(d), the intrinsic lifetimes for 46 GHz and 105 are even close to each other and seem independent of frequency. They still do not follow the relation $\tau_P^{-1} \propto f^2$.

The deviation from the relation $\tau_P^{-1} \propto f^2$ implies that $\tau_{\text{in}}^{-1} \propto f^2$, or $\tau_{\text{ex}}^{-1} \propto f^4$, or both break down in the frequency range above 46 GHz. One may speculate that $\tau_{\text{ex}}^{-1} \propto f^4$ might not be a proper assumption because point defects may not dominate the defect scatterings in STO. More general

conditions are considered as follows:

$$\tau_p^{-1}(f_1) = \tau_{\text{in}}^{-1}(f_1) + \tau_{\text{ex}}^{-1}(f_1)$$
$$\tau_p^{-1}(f_2) = \tau_{\text{in}}^{-1}(f_2) + \tau_{\text{ex}}^{-1}(f_2), \quad (7)$$

where $f_1 = 105\,\text{GHz}$ and $f_2 = 46\,\text{GHz}$. $\tau_p^{-1}(f_1)$ and $\tau_p^{-1}(f_2)$ are the as measured experimental data in Figs. 4(b) and 5(d), respectively. If we assume that $\tau_{\text{in}}^{-1} \propto f^2$ is still valid and the relation associated with the defect scatterings is $\tau_{\text{ex}}^{-1} \propto f^a$, Eq. (7) leads to the results that the power a of f is less than one. It should be noted that line defects and point defects result in the relations $\tau_{\text{ex}}^{-1} \propto f^2$ and $\tau_{\text{ex}}^{-1} \propto f^4$, respectively. For an imperfect crystal with both types of defects, the power a should be within 2 and 4 from the statistical analysis of experimental data. However, the obtained relation, $\tau_{\text{ex}}^{-1} \propto f^a$ with $a < 1$, is beyond our knowledge to have a physical picture accounting for the defect scatterings. Our experimental results and statistical analysis suggest that the intrinsic phonon lifetime between 46 GHz and 105 GHz already deviates from the relation $\tau_{\text{in}}^{-1} \propto f^2$. Actually, similar phenomena were also observed in GaAs-based semiconductors [47]. Although Akhiezer model yields a quadratic frequency dependence, the phonon lifetime of GaAs starts to deviate from the quadratic dependence above ∼20 GHz and becomes independent of frequency (constant value). In our work, the intrinsic phonon lifetimes of STO at ∼50 and ∼100 GHz are both around 400–500 ps. An adequate theory is required to quantitatively account for this phenomenon both in GaAs and STO.

Finally, we conducted probe-wavelength-dependent experiments to address the disagreements for optical constants of STO in previous measurements [32,33]. Because the dispersion relation for longitudinal acoustic phonon in STO has been confirmed linear within our experimental conditions [48], the sound velocity can be assumed constant in Eq. (4) as a function of probe wavelength and its corresponding Brillouin frequency. Following Eq. (4), we used 7.9 nm/ps as the sound velocity to obtain the refractive index. Our obtained refractive index for probe wavelength 800 nm agrees well with that from Ref. [32], rather than that from Ref. [33]. By varying the wavelengths of pump/probe, we determined the refractive index of STO from 400 to 365 nm as shown in Fig. 6, which was not measured in Ref. [32].

IV. SUMMARY

We utilized ultrafast pump-probe spectroscopy to generate and detect hypersound in $SrRuO_3/SrTiO_3$ heterostructures. We found that the efficiency of generating hypersound in SRO, through thermal expansion, is linear up to optical fluence of a few mJ/cm^2. The temperature dependence of hypersound dynamics in STO substrate revealed that the acoustic properties of STO dramatically changed around the temperature of structural transition (105 K). Although the mode-coupling theory could still qualitatively account for the acoustic properties of STO in GHz regime, the quadratic frequency dependence of phonon lifetime breaks down at tens of GHz. Finally, we determined the refractive index of STO from 400 to 365 nm, for which there was disagreement in previous results.

ACKNOWLEDGMENTS

The authors acknowledge Dr. Ajay K. Yadav, Prof. Ramamoorthy Ramesh, UC Berkeley, and Dr. Yu-Chieh Wen, Academia Sinica, for providing us the sample. The authors also thank Dr. Chia-Hao Hsu and Prof. Maw-Kuen Wu, Academia Sinica for x-ray measurements of the samples to check the structural transition temperature of STO. This work is sponsored by Ministry of Science and Technology of Taiwan under Grants No. 104-2112-M-001-014-MY3 and No. 107-2119-M-001-046.

[1] H. Ohta, S. Kim, Y. Mune, T. Mizoguchi, K. Nomura, S. Ohta, T. Nomura, Y. Nakanishi, Y. Ikuhara, M. Hirano, H. Hosono, and K. Koumoto, Nat. Mater. **6**, 129 (2007).
[2] A. Ohtomo and H. Y. Hwang, Nature **427**, 423 (2004).
[3] F. W. Lytle, J. Appl. Phys. **35**, 2212 (1964).
[4] C. Ang, J. F. Scott, Z. Yu, H. Ledbetter, and J. L. Baptista, Phys. Rev. B **59**, 6661 (1999).
[5] K. Fossheim and B. Berre, Phys. Rev. B **5**, 3292 (1972).
[6] E. R. Domb, H. K. Schurmann, and T. Mihalisin, Phys. Rev. Lett. **36**, 1191 (1976).
[7] R. Nava, R. Callarotti, H. Ceva, and A. Martinet, Phys. Rev. **188**, 1456 (1969).
[8] S. Lee, B. A. Apgar, and L. W. Martin, Adv. Energy Mater. **3**, 1084 (2013).
[9] C. v. Korff Schmising, A. Harpoeth, N. Zhavoronkov, Z. Ansari, C. Aku-Leh, M. Woerner, T. Elsaesser, M. Bargheer, M. Schmidbauer, I. Vrejoiu, D. Hesse, and M. Alexe, Phys. Rev. B **78**, 060404(R) (2008).
[10] M. Herzog, A. Bojahr, J. Goldshteyn, W. Leitenberger, I. Vrejoiu, D. Khakhulin, M. Wulff, R. Shayduk, P. Gaal, and M. Bargheer, Appl. Phys. Lett. **100**, 094101 (2012).
[11] R. Shayduk, M. Herzog, A. Bojahr, D. Schick, P. Gaal, W. Leitenberger, H. Navirian, M. Sander, J. Goldshteyn, I. Vrejoiu, and M. Bargheer, Phys. Rev. B **87**, 184301 (2013).
[12] A. Bojahr, D. Schick, L. Maerten, M. Herzog, I. Vrejoiu, C. von Korff Schmising, C. Milne, S. L. Johnson, and M. Bargheer, Phys. Rev. B **85**, 224302 (2012).
[13] A. Bojahr, M. Herzog, D. Schick, I. Vrejoiu, and M. Bargheer, Phys. Rev. B **86**, 144306 (2012).
[14] K. J. Manke, A. A. Maznev, C. Klieber, V. Shalagatskyi, V. V. Temnov, D. Makarov, S. H. Baek, C. B. Eom, and K. A. Nelson, Appl. Phys. Lett. **103**, 173104 (2013).
[15] H. J. Liu, L. Y. Chen, Q. He, C. W. Liang, Y. Z. Chen, Y. S. Chien, Y. H. Hsieh, S. J. Lin, E. Arenholz, C. W. Luo, Y. L. Chueh, Y. C. Chen, and Y. H. Chu, ACS Nano **6**, 6952 (2012).
[16] H. J. Liu, T. C. Wei, Y. M. Zhu, R. R. Liu, W. Y. Tzeng, C. Y. Tsai, Q. Zhan, C. W. Luo, P. Yu, J. H. He, Y. H. Chu, and Q. He, Adv. Funct. Mater. **26**, 729 (2016).
[17] C. Thomsen, J. Strait, Z. Vardeny, H. J. Maris, J. Tauc, and J. J. Hauser, Phys. Rev. Lett. **53**, 989 (1984).
[18] C. Thomsen, H. T. Grahn, H. J. Maris, and J. Tauc, Phys. Rev. B **34**, 4129 (1986).

[19] H. T. Grahn, H. J. Maris, and J. Tauc, IEEE J. Quantum Electron. **25**, 2562 (1989).
[20] N. Akira, Y. Akihiro, T. Kenichi, O. Hirotsugu, N. Nobutomo, and H. Masahiko, Jpn. J. Appl. Phys. **51**, 07GA09 (2012).
[21] F. J. Wei, Y.-H. Yeh, J.-K. Sheu, and K.-H. Lin, Sci. Rep. **6**, 28577 (2016).
[22] C. K. Sun, J. C. Liang, C. J. Stanton, A. Abare, L. Coldren, and S. P. DenBaars, Appl. Phys. Lett. **75**, 1249 (1999).
[23] C. K. Sun, J. C. Liang, and X. Y. Yu, Phys. Rev. Lett. **84**, 179 (2000).
[24] K. H. Lin, C. M. Lai, C. C. Pan, J. I. Chyi, J. W. Shi, S. Z. Sun, C. F. Chang, and C. K. Sun, Nat. Nanotechnol. **2**, 704 (2007).
[25] Y. C. Wen, L. C. Chou, H. H. Lin, V. Gusev, K. H. Lin, and C. K. Sun, Appl. Phys. Lett. **90**, 172102 (2007).
[26] A. A. Maznev, K. J. Manke, K. H. Lin, K. A. Nelson, C. K. Sun, and J. I. Chyi, Ultrasonics **52**, 1 (2012).
[27] A. Bartels, T. Dekorsy, H. Kurz, and K. Köhler, Phys. Rev. Lett. **82**, 1044 (1999).
[28] K. Mizoguchi, M. Hase, S. Nakashima, and M. Nakayama, Phys. Rev. B **60**, 8262 (1999).
[29] K. H. Lin, G. W. Chern, C. T. Yu, T. M. Liu, C. C. Pan, G. T. Chen, J. I. Chyi, S. W. Huang, P. C. Li, and C. K. Sun, IEEE Trans. Ultrason. Ferroelectr. Freq. Control **52**, 1404 (2005).
[30] T.-C. Wei, H.-P. Wang, H.-J. Liu, D.-S. Tsai, J.-J. Ke, C.-L. Wu, Y.-P. Yin, Q. Zhan, G.-R. Lin, Y.-H. Chu, and J.-H. He, Nat. Commun. **8**, 15018 (2017).
[31] F. Schwabl, Phys. Rev. B **7**, 2038 (1973).
[32] M. Cardona, Phys. Rev. **140**, A651 (1965).
[33] D. Bäuerle, W. Braun, V. Saile, G. Sprüssel, and E. E. Koch, Z. Phy. B-Condens. Mat. **29**, 179 (1978).
[34] S. Yamanaka, T. Maekawa, H. Muta, T. Matsuda, S. Kobayashi, and K. Kurosaki, J. Solid State Chem. **177**, 3484 (2004).
[35] A. G. Beattie and G. A. Samara, J. Appl. Phys. **42**, 2376 (1971).
[36] D. W. Oh, J. Ravichandran, C. W. Liang, W. Siemons, B. Jalan, C. M. Brooks, M. Huijben, D. G. Schlom, S. Stemmer, L. W. Martin, A. Majumdar, R. Ramesh, and D. G. Cahill, Appl. Phys. Lett. **98**, 221904 (2011).
[37] O. Matsuda and O. B. Wright, J. Opt. Soc. Am. B **19**, 3028 (2002).
[38] R. L. Liu, G. D. Sanders, C. J. Stanton, C. S. Kim, J. S. Yahng, Y. D. Jho, K. J. Yee, E. Oh, and D. S. Kim, Phys. Rev. B **72**, 195335 (2005).
[39] L. Braic, N. Vasilantonakis, B. Zou, S. A. Maier, N. M. Alford, A. V. Zayats, and P. K. Petrov, Sci. Rep. **5**, 9118 (2015).
[40] K. H. Lin, K. J. Wang, C. C. Chang, Y. C. Wen, B. Lv, C. W. Chu, and M. K. Wu, Sci. Rep. **6**, 25962 (2016).
[41] S. Zollner, A. A. Demkov, R. Liu, P. L. Fejes, R. B. Gregory, P. Alluri, J. A. Curless, Z. Yu, J. Ramdani, R. Droopad, T. E. Tiwald, J. N. Hilfiker, and J. A. Woollam, J. Vac. Sci. Technol. B **18**, 2242 (2000).
[42] A. Devos, M. Foret, S. Ayrinhac, P. Emery, and B. Ruffle, Phys. Rev. B **77**, 100201 (2008).
[43] A. Dejneka, M. Tyunina, J. Narkilahti, J. Levoska, D. Chvostova, L. Jastrabik, and V. A. Trepakov, Phys. Solid State **52**, 2082 (2010).
[44] T. Toyoda and M. Yabe, J. Phys. D - Appl. Phys. **16**, L251 (1983).
[45] E. D. Mishina, A. I. Morozov, A. S. Sigov, N. E. Sherstyuk, O. A. Aktsipetrov, V. V. Lemanov, and T. Rasing, J. Exp. Theor. Phys. **94**, 552 (2002).
[46] G. Shirane and Y. Yamada, Phys. Rev. **177**, 858 (1969).
[47] A. A. Maznev, F. Hofmann, A. Jandl, K. Esfarjani, M. T. Bulsara, E. A. Fitzgerald, G. Chen, and K. A. Nelson, Appl. Phys. Lett. **102**, 041901 (2013).
[48] A. Devos, Y.-C. Wen, P.-A. Mante, and C.-K. Sun, Appl. Phys. Lett. **100**, 206101 (2012).